Numerical and experimental investigation of CdZnTe growth by the boron oxide encapsulated vertical Bridgman method

Carmen Stelian, Davide Calestani, Matias Velázquez, Andrea Zappettini

Numerical and experimental investigation of CdZnTe growth by the boron oxide encapsulated vertical Bridgman method

Carmen Stelian[1*], Davide Calestani[2], Matias Velázquez[1], Andrea Zappettini[2]

[1]*Université Grenoble Alpes, CNRS, Grenoble INP, SIMAP, 1340 Rue de la Piscine, F-38402, Saint Martin d'Hères, France*

[2]*IMEM-CNR, Parco Area delle Scienze 37/A, 43124, Parma, Italy*

**Corresponding author: Carmen Stelian, Address: SIMAP-EPM, 1340 Rue de la Piscine, BP 75, 38402 Saint Martin d'Hères, France, Fax:* +33 4 76 82 52 49*; Tel:* +33 4 76 82 52 56*; E-mail: steliancarmen@yahoo.com*

Abstract

Cadmium zinc telluride crystals of 4.8 cm in diameter grown by the boron oxide encapsulated vertical Bridgman technique exhibit good structural quality with large grains and low dislocation density. However, the ingots contain Te inclusions, which are trapped at the growth interface during the crystallization process. Global modeling of the furnace was applied in order to investigate the temperature gradients and the evolution of the growth interface shape in this system. Transient computations, which include the crucible movement, show that the crystal-melt interface is concave toward the melt in the conical part of the ampoule, then becomes convex during the growth in the cylindrical part of the ampoule. Concave shapes of the interface and very homogeneous temperature distribution at the beginning of the solidification process promote the growth of a polycrystalline material. A novel hypothesis explaining the mechanism of grains formation at the ampoule tip was formulated. Our calculations show that the anomalous Zn segregation is due to the poor solute mixing at the beginning of the solidification process. The modeling of the standard growth process reveals very low vertical temperature gradients in the crystal (2-4 K/cm). Such low temperature gradients are

not favorable to eliminate the Te inclusions in the as grown crystal. A numerical model was employed to analyze the temperature field influence on the migration/size reduction of Te inclusions.

Keywords: Semiconducting II-VI materials, Computer simulation, Bridgman technique

1. Introduction

CdZnTe (CZT) is one of the leading materials used for infrared, X-ray and γ-ray detectors [1-3]. The performance of CZT detectors depends on the quality of the crystalline material. The commercial applications of CZT are limited by the presence of some material defects as the grains boundaries, dislocations, inclusions and non-homogeneous Zn distribution.

Bridgman growth of CdTe and CdZnTe crystals have been extensively studied by means of experiments and numerical modeling [4-10]. It was found that slightly convex (towards liquid phase) shapes of the crystal-melt interface promote the growth of good quality crystals. On the contrary, too concave interface shapes at the start of the crystallization process lead to multiple grains formation. Several papers [6,9] have been dedicated to the optimization of the temperature field in Bridgman furnaces, with the aim of controlling the interface shape during the growth process.

Good quality CZT crystals were grown by the encapsulated vertical Bridgman technique in a three zone furnace. The experimental technique is described in [11-14]. Before growth, the charge with a zinc concentration of 10% was doped with indium, with the aim of getting high resistivity CZT used for X-ray detector applications. During growth, the charge was covered by a liquid boron oxide layer that prevents the contact between the growing crystal and the ampoule walls. The ingots of 4.8 cm in diameter grown in this configuration exhibit very low dislocation densities ($10^3 - 10^4\ cm^{-2}$) and few large grains. However, the presence of Te inclusions in the crystals is a major issue for the quality of this material. The inclusions of size larger than 1 μm are trapped at the crystal-melt interface during the solidification process [15]. It is supposed that low vertical gradients across the solid CZT sample during the growth process are not favorable for eliminating the Te droplets.

In this work, numerical modeling is applied to investigate the temperature gradients, the evolution of the growth interface shape and the Zn distribution in CdZnTe crystals grown by the encapsulated vertical Bridgman method. A novel numerical model was employed to simulate the migration of Te inclusions under the influence of a vertical temperature gradient.

2. Numerical model

The modeling is conducted for the crystallization experiments performed in a three zone vertical Bridgman furnace [11-14]. $Cd_{1-x}Zn_xTe$ (x=10%) crystals of 4.8 cm in diameter and about 7 cm in length were grown in cylindrical quartz ampoules having a conical tip. After the charge melting, the ampoule is moved down at 0.5-2 mm/h rate. The charge is fully encapsulated by a boron oxide layer of 100-200 μm in thickness.

Global modeling of the furnace is performed by using the finite element code COMSOL Multiphysics. The coupled equations of heat transfer, momentum and species transport are solved in an axisymmetric domain (Fig. 1). The shape of the crystal-melt interface and the crucible movement are computed by applying a deformable mesh technique. The heat transfer includes thermal exchanges by conduction and wall-to-wall radiation. The gas convection effect is simulated by introducing an increased thermal conductivity of the inert gas. The flow computations include the buoyancy convection in the melt.

The segregation of Zn at the crystal-melt interface is described by the following equation:

$$\phi = -D \cdot \nabla C \cdot \vec{n} = (1 - K) \cdot (\vec{V} \cdot \vec{n}) \cdot C_I \quad (1)$$

where ϕ, D, K, C_I, $\vec{V}$ and $\vec{n}$ are the solute mass flux, diffusion coefficient, segregation coefficient, species concentration in the liquid at the interface, growth rate and the normal vector at the interface, respectively.

More details about modeling the Bridgman growth of CZT are given in a previous work [16].

3. Results

3.1 Standard growth process

Figure 1 shows the numerical results at the beginning (Fig. 1a) and by the end (Fig.1b) of the growth process. The power supplied in the resistive heaters is considered constant during the crystallization process.

The ampoule is moved down at constant rate $V_T = 2\,mm/h$. The transient computations show that the solidification rate ($V_S \cong 0.5\,mm/h$) is smaller than the translation rate of the ampoule. Since the computations with deformable mesh are not convergent when the solidification front arrives at the top of the conical part of the ampoule, the modeling of the growth in the cylindrical part of the ampoule is performed by starting a new computation with an initial flat shape of the crystal-melt interface.

Temperatures are very homogeneous in the solid-liquid sample (see the left side of the images in Fig. 1a and 1b). The vertical temperature gradients in the crystal near the solidification interface are very low: $G_S \cong 1K/cm$ at the beginning of the growth process and, respectively, $G_S \cong 4K/cm$ for the solidification in the cylindrical part of the ampoule. The crystal-melt interface is concave toward the melt in the conical part of the ampoule, then becomes slightly convex in the cylindrical part of the ampoule. The flow pattern exhibits two opposite vortices during the early stages of the growth, and only one flow cell by the end of the crystallization process (see the right side of Fig. 1a and Fig. 1b).

Fig. 2 shows the evolution of the velocity field (left side) and Zn concentration (right side) during the solidification in the conical part (Fig. 2a) and the cylindrical part (Fig. 2b) of the ampoule. The blue line represents the solidification isotherm. At the beginning of the crystallization process (time $t = 0.5\,h$), the crystal-melt interface is concave with a large curvature (interface deflection $f = 0.33\,cm$). The melt flow consists of two opposite vortices. The first one is located in the conical region, with the liquid flowing upward along the symmetry axis, while the second one is weaker and located in the cylindrical region of the ampoule. The maximum flow velocity is located near the ampoule wall: $u_{max} = 5.28 \cdot 10^{-4} m/s$. The left part of the image shows the dimensionless Zn concentration (C/C_0). The iso-concentrations are significantly distorted by the flow in the region adjacent to the growth interface. The radial segregation at the crystal-melt interface is estimated by the following formula:

$$\delta C = \frac{C_{max} - C_{min}}{C_{av}} \tag{2}$$

where C_{max}, C_{min} and C_{av} are the maximum, the minimum and the average concentrations in the liquid along the growth interface. The value computed at $t = 0.5\,h$ is $\delta C = 0.07$ (C_{min} and C_{max} are located at the center and near the ampoule wall, respectively).

The results plotted for the solidification times $t = 4.2\ h$ and $t = 6.6\ h$ show that the shape of the crystal-melt interface remains concave during the crystallization in the conical part of the ampoule (Fig. 2a). The interface deflection increases to $f = 0.6\ cm$ at $t = 4.2\ h$, then decreases to $f = 0.5\ cm$ at $t = 6.6\ h$. The flow pattern and the concentration field are only slightly changed during the growth in the conical part of the ampoule. The maximum flow velocity decreases to $u_{max} = 4.67 \cdot 10^{-4} m/s$ at $t = 6.6\ h$.The radial segregation decreases from $\delta C = 0.045$ at $t = 4.2\ h$ to $\delta C = 0.03$ at $t = 6.6\ h$.

Fig. 2b shows that the crystal-melt interface is still concave shaped at the beginning of the solidification in the cylindrical part of the ampoule. The values of the interface deflection and radial segregation at time $t = 9\ h$ are respectively: $f = 0.4\ cm$ and $\delta C = 0.03$. The shape of the crystal-melt interface is almost flat at $t = 17.6\ h$, then becomes slightly convex. The flow pattern is changed at $t = 17.6\ h$ exhibiting one single vortex extended in the whole volume of the melt. The liquid rises along the ampoule wall and downwards along the symmetry axis. The change in the flow pattern generates large radial segregation at $t = 17.6\ h$ ($\delta C = 0.2$). The interface become convex shaped after $18\ h$ of crystallization and the radial segregation decreases: $f = -0.1\ cm$ and $\delta C = 0.04$ at $t = 61\ h$.

Fig. 3 compares the measured Zn concentration profile to the numerical results. Measurements of Zn distribution in CZT crystals grown with and without encapsulation have been performed by means of the photoluminescence mapping in a previous work [14]. The measured Zn concentration profile along the symmetry axis of the ingot show anomalous segregation. The concentration increases in the first part of the ingot (solidified fraction $f_S \leq 0.15$), then decreases toward the crystal tail. The numerical computations are started at the solidified fraction $f_S = 0.1$ by considering a homogeneous initial zinc distribution in the melt ($C_0 = 10\%$). The computed Zn distribution along the crystal axis is in agreement with the measured profile (Fig. 3). Numerical computations with deformable mesh were convergent until $f_S = 0.9$.

The anomalous Zn segregation could be explained as a result of the poor solute mixing at the bottom part of the ampoules having a sharp conical tip. Fig. 4 shows the dimensionless concentration field (C/C_0), Zn isoconcentrations and the velocity field at the beginning of the solidification process. The solutal mass flux has a maximum at the interface center ($\vec{V} \cdot \vec{n} = V$) and a minimum near the crucible wall ($\vec{V} \cdot \vec{n} = V \cdot cos\varphi$, where φ is the angle between the normal vector at the interface and the growth direction). Therefore, Zn

concentration in the melt decreases more rapidly at the interface center than near the ampoule wall. If the conical part of the ampule is sharp, the convection is weak at the center of the growth interface. The poor solute mixing generates a stratified composition of the melt, with increasing Zn concentration along the symmetry axis (see Fig. 4). The crystallization of a liquid with a stratified Zn composition leads to anomalous segregation behavior.

The grains formation at the beginning of the crystallization process is explained in Fig. 5. The radial variation of Zn concentration along the crystal-melt interface is significant at the beginning of the growth process. The non-uniform Zn distribution along the crystallization front influences the solidification temperature, which is given by the formula:

$$T_S(C_I) = T_S^0 + m_L \cdot C_I \quad (3)$$

In the above formula T_S^0 is the solidification temperature of CdTe ($T_S^0 = 1365\ K$), m_L is the liquidus slope ($m_L = 1.8\ K/\%$) and C_I is the concentration in the liquid at the growth interface.

If the crystallization occurs under low vertical temperature gradient ($G_L = 1K/cm$ at the beginning of the growth process), even small variations of the solidification temperature can generate a distorted shape of the interface and promote grains formation. The computed shapes of the growth interface carried out from simulations which neglect and, respectively, account for the dependence of the melting point on the Zn concentration are shown in Fig. 5a and b. The case computed by neglecting the liquidus effect shows a concave shaped interface ($f = 0.25\ cm$) at the beginning of the solidification process (Fig. 5a). Significant variation of Zn concentration is observed along the growth interface: $(C/C_0)^{min} = 0.97$ at the liquid center and $(C/C_0)^{max} = 1$ near the ampoule wall. As the temperature increases along the vertical direction, the liquid at higher Zn content (high T_S) adjacent to the ampoule wall reaches the solidification temperature and crystalizes at the same time as the melt of lower Zn content (low T_S) located at the center of the tip. The computation performed by accounting the liquidus effect shows that the crystallization starts simultaneously at the center of the tip and from the ampoule wall (Fig. 5b). These results are in agreement with the experiments showing that large grains develop from the bottom part of the ampoule (Fig. 5c). The computations with deformable mesh which account for the liquidus effect can be conducted only at the beginning of the

crystallization process. This kind of computations becomes divergent when the interface shape is too distorted. Therefore, the modeling of the full crystallization process was performed by neglecting the liquidus effect.

Numerical computations of the crystal-melt interface shape are compared to previous experimental measurements [13]. In this experimental work, the growth interface shape was studied by means of photoluminescence mapping. The crystals grown by the encapsulated Bridgman method were cut parallel to the growth direction, then scanned by a laser beam. The peak energy was then converted into zinc content. This procedure allows the zinc concentration mapping in the samples. The isoconcentrations were interpreted as showing the growth interface shape.

Fig. 6 shows the concentration field and isoconcentration contours computed for two solidified fractions: $f_S = 0.29$ (Fig. 6a) and $f_S = 0.55$ (Fig. 6b). It can be observed that the isoconcentration contours are significantly deformed by the convection at the beginning of the solidification in the cylindrical part of the ampoule ($f_S = 0.29$). In this case, the lines of constant concentration cannot be interpreted as showing the interface shape. The results obtained at $f_S = 0.55$ show that the solutal field is less affected by the convection, so, in this case, the isoconcentrations follow the interface shape. The computed interface deflection $f \cong 1\ mm$ (at $f_S = 0.55$) is in good agreement with the experimental result carried out from the photoluminescence mapping [13].

3.2 Migration of Te inclusions

The results presented in the previous section reveal low vertical temperature gradients (2-4 K/cm) in the solid-liquid sample during the crystallization process. It is supposed that such low temperature gradients are not favorable for the elimination/reduction of Te precipitates in CZT crystals.

In the followings, numerical modeling is employed to analyze the influence of temperature conditions on Te droplets migration/elimination. The simulation domain contains a Te inclusion of $30\ \mu m$ in diameter and the surrounding solid sample of $2\ mm$ in thickness. Time dependent heat transfer and species equations are solved in a 2D axisymmetric domain. Solute segregation at the solid-liquid interface is described by Eq. 1. The melting point dependence on Te concentration (Eq. 3) is taken into account in these computations. The

values of the segregation coefficient ($K = 0.55$) and the liquidus slope ($m_L = -8K/\%$) are taken from the phase diagram of CdTe [17]. The simulations are started with the following initial concentrations of tellurium: $\mathrm{C_{Te}}(\mathrm{inclusion}) = 100\%$ and $\mathrm{C_{Te}}(\mathrm{solid}) = 50\%$. The shape of moving Te inclusions is computed by using the deformable mesh technique. Computations are performed with different values of the vertical temperature gradient: $G_S = 8K/cm$ (Fig. 7a), $G_S = 2K/cm$ (Fig. 7b) and $G_S = 0.1K/cm$ (Fig. 7c). The temperature increases linearly to the upper part of the simulation domain with a maximum of $1360\ K$ at the top surface.

The migratory mechanism of Te inclusions under the influence of a temperature gradient was explained by Vydyanath et al. [18] It was found that at temperatures higher than $723\ K$, the Te inclusions are in the liquid state and dissolve the surrounding solid CdZnTe. As the layer around the inclusion is enriched in Te, the solidification temperature of CdZnTe decreases (according to Eq. 3).Therefore, the solid at the hot part of the inclusion (top end) is melted, while the cold part of the inclusion (bottom end) is solidified. If the temperature difference between the bottom and the top part of the inclusion is high enough, the droplet migrates towards the high temperature zone.

Fig. 7a shows numerical results obtained in the case of high temperature gradient $G_S = 8K/cm$. The transient computations with deformable mesh are not convergent after $t = 1800\ s$ since the droplet shape becomes too distorted. The results plotted at times $t = 0s$ and $t = 1800\ s$ reveal that the inclusion moves towards the top surface of the simulation domain. The time evolution of z-coordinate at the bottom and, respectively, at the top part of the droplet is plotted at the right side of the figure. Numerical results show that the droplet moves up with an average velocity of $10^{-8}m/s$. The droplet diameter decreases from $30\ \mu m$ ($t = 0\ s$) to $26\ \mu m$ ($t = 1800\ s$).

Numerical results carried out from the simulation with $G_S = 2K/cm$ (the average vertical temperature gradient in the solid sample during the crystallization process) are shown in Fig. 7b. In this case, the temperature difference across the droplet is not high enough to trigger an efficient migration mechanism. The time evolution of z-coordinate reveals a low migration rate ($2 \cdot 10^{-9}m/s$) and only a small reduction of the droplet diameter ($29\ \mu m$ at $t = 1800\ s$).

The computation performed with $G_S = 0.1K/cm$ shows that there are no changes in either the size or the position of the droplet (Fig. 7c).

The influence of the ingot temperature on the migration/elimination mechanism of Te inclusions is analyzed in Fig. 8. The computations are performed with two temperatures: $T = 1360\,K$ (the average temperature of the solid sample during the crystallization process) and $T = 1000\,K$ (temperature reached during the cooling down process). The applied temperature gradient is $G_S = 6K/cm$. Numerical results obtained in the case of high ingot temperature ($T = 1360\,K$) reveal that the Te droplet moves up with an average velocity of $10^{-8}m/s$ (Fig. 8a). The droplet size is slightly reduced from 30 μm ($t = 0\,s$) to 28.3 μm ($t = 1100\,s$). These results show that the migration/elimination mechanism of Te inclusions is not efficient at high temperatures reached during the crystallization process. On the contrary, the elimination mechanism becomes effective at temperatures around $1000\,K$ reached during the cooling down stage of the elaboration process. The results plotted in Fig. 8b show that the droplet size is reduced to $0.5\,\mu m$ at $t = 2700\,s$. The inclusion is also moving up with an average velocity of $3 \cdot 10^{-9}m/s$.

These numerical results are in agreement with the results obtained in experimental annealing of CZT wafers under a temperature gradient. Several experimental works [19,20] have shown that the elimination efficiency of Te inclusions after annealing under a temperature gradient of $7 - 8\,K/cm$ increases largely at annealing temperatures around $1015\,K$.

3.3 Modified growth process

According to previous numerical results, the growth process should be modified in order to allow the elimination of Te inclusions, which becomes effective under a temperature gradient of about $6\,K/cm$ applied at temperatures around $1000\,K$.

In the standard growth process, the crystallization is ended when the ampoule is positioned at the top part of the second heat zone (see Fig. 9a). The computed vertical temperature gradient along the symmetry axis of the ingot is shown at the right side of the figure. The average value of G_S in the cylindrical part of the ingot is about $4.5\,K/cm$. The temperature gradient reaches $6\,K/cm$ only at the top part of the ingot. In the Fig. 9b, the ampoule was lowered down by $1.5\,cm$, in order to increase the average temperature gradient in the cylindrical part of the ingot to $6.5\,K/cm$. The mean temperature of the ingot is $1230\,K$. At this stage of

the elaboration process, the temperature should be decreased to $1000\ K$ by keeping the ampoule in the same position. After $1\ h$ annealing at $1000\ K$, the ingot may be cooled down to the ambient temperature.

4 Conclusions

Numerical modeling was applied to investigate the temperature gradients, the shape of the crystal-melt interface and Zn distribution in CZT crystal growth by the encapsulated Bridgman technique. This work presents for the first time numerical results carried out from a global modeling of this kind of furnace that includes also the ampoule translation and tracking of the growth interface.

Transient simulations of the complete solidification process show that the solid-liquid interface is concave shaped at early stages of the growth and becomes convex shaped by the end of the crystallization process. These results are in agreement with previous experimental characterization of the crystals by means of photoluminescence mapping showing convex shapes of the interface in the cylindrical part of the ampoule. The modeling shows that Zn isoconcentrations reveal the crystal-melt interface shape only at the upper half of the ingot (solidified fraction $f_S \geq 0.5$).

A novel hypothesis explaining the anomalous Zn segregation observed in experiments was proposed. The increasing concentration profile in the first part of the crystal could be explained by the poor mixing of the solute at the ampoule tip, which leads to a stratified composition of the melt in the vicinity of a concave shaped growth interface.

A mechanism explaining the grains formation at the beginning of the solidification process was proposed and validated by comparing the numerical results to the experimental observations.

The results obtained from modeling the crystallization process reveal low vertical temperature gradients in the solid sample, which are not favorable for the elimination of Te precipitates at high

temperatures. Numerical modeling of Te inclusions migration in the solid CZT shows that the droplets elimination mechanism is effective under a vertical temperature of $6\,K/cm$ applied at temperatures around $1000\,K$. The elaboration process should be accordingly modified in order to allow the Te inclusions elimination during the cooling down stage.

References

[1] K. Sato, Y. Seki, Y. Matsuda, O. Oda, J. Cryst. Growth 197 (1999) 413.

[2] M. Fiederle, T. Feltgen, J. Meinhardt, M. Rogalla, K.W. Benz, J. Cryst. Growth 197 (1999) 635.

[3] P. Rudolph, Prog. Cryst. Growth Charact. 29 (1994) 275.

[4] V. Carcelén, K.H. Kim, G.S. Camarda, A.E. Bolotnikov, A. Hossain, G. Yang, J. Crocco, H. Bensalah, F. Dierre, E. Dieguez, R.B. James, J. Cryst. Growth 338 (2012) 1.

[5] V. Komar, A. Gektin, D. Nalivaiko, I. Klimenko, V. Migal, O. Panchuk, A. Rybka, Nucl. Instr. and Meth. A 458 (2001) 113.

[6] S. Kuppurao, J.J. Derby, J. Cryst. Growth 172 (1997) 350.

[7] S. Kuppurao, S. Brandon, J.J. Derby, J. Cryst. Growth 155 (1995) 93.

[8] C. Martinez-Tomas, V. Munoz, R. Triboulet, J. Crystal Growth 197 (1999) 435.

[9] D. Gasperino, M. Bliss, K. Jones, K. Lynn, J.J. Derby, J. Crystal Growth 311 (2009) 2327.

[10] J. J. Derby, N. Zhang, A. Yeckel, J. Crystal Growth 379 (2013) 28.

[11] A. Zappettini, M. Zha, M. Pavesi, L. Zanotti, J. Crystal Growth 307 (2007) 283–288.

[12] M. Zha, A. Zappettini, D. Calestani, L. Marchini, L. Zanotti, C. Paorici, J. Crystal Growth 310 (2008) 2072–2075

[13] A. Zappettini, M. Zha, L. Marchini, D. Calestani, CrystEngComm 14 (2012) 5992–5995.

[14] A. Zappettini, L. Marchini, M. Zha, G. Piacentini, N. Zambelli, G. Benassi, D. Calestani, CrystEngComm 15 (2013) 2227.

[15] A. Zappettini, N. Zambelli, G. Benassi, D. Calestani, M. Pavesi, Appl. Phys. Lett. 104 (2014) 252105.

[16] C. Stelian, T. Duffar, J. Crystal Growth 446 (2016) 42.

[17] J. H. Greenberg, J. Cryst. Growth 161 (1996) 1.

[18] H. Vydyanath, J. Ellsworth, J. B. Parkinson, et al., J. Electron. Mater. 22 (1993) 1073.

[19] Y. He, W. Jie, T. Wang, Y. Xu, Y. Zhou, Y. Zaman, G. Zha, J. Crystal Growth 402 (2014) 15.

[20] G. Yang, A. E. Bolotnikov, P. M. Fochuk, et al., J. Crystal Growth 379 (2013) 16.

(a)

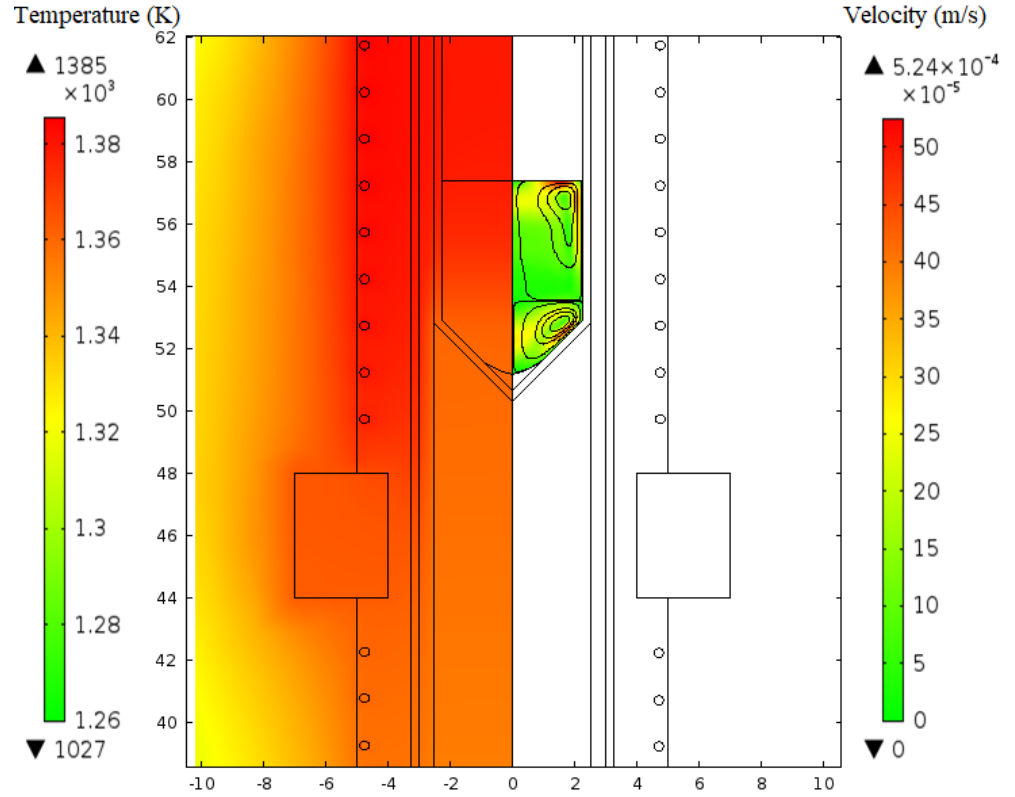

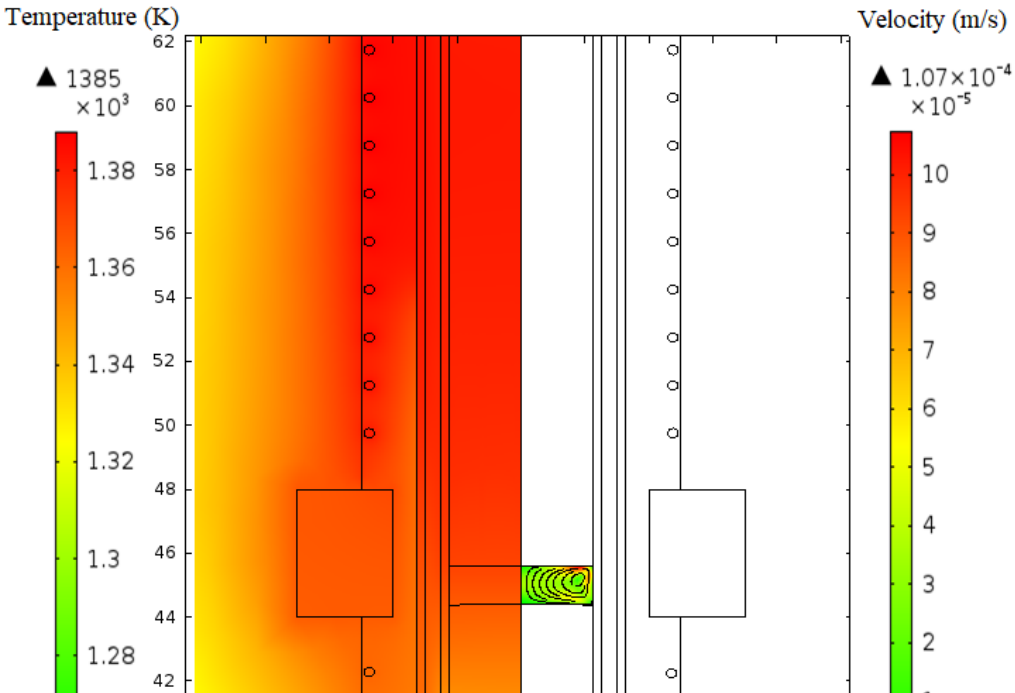

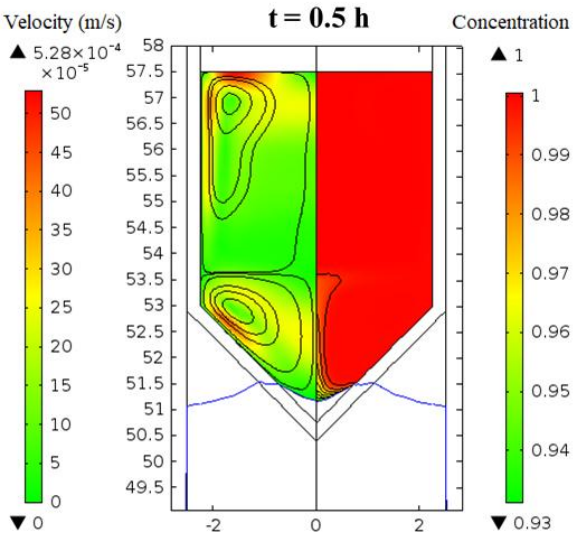
t = 0.5 h
Velocity (m/s)
Concentration

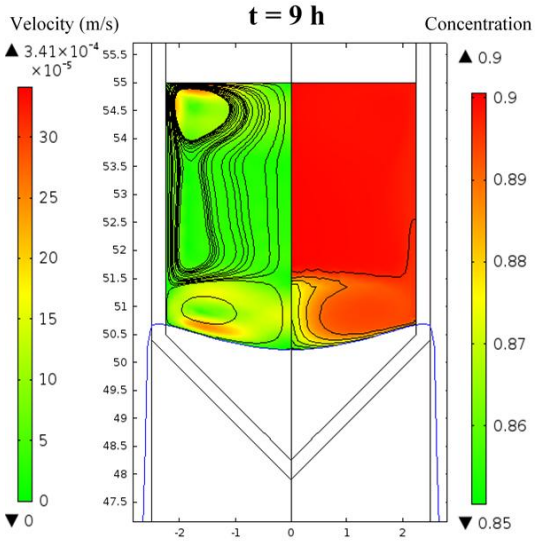
t = 9 h
Velocity (m/s)
Concentration

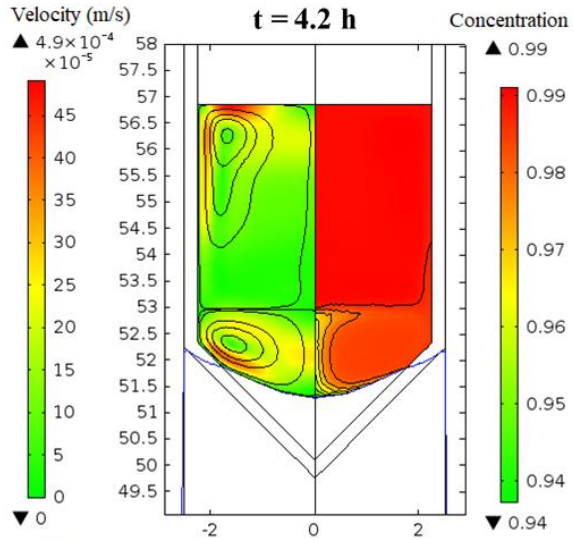
t = 4.2 h
Velocity (m/s)
Concentration

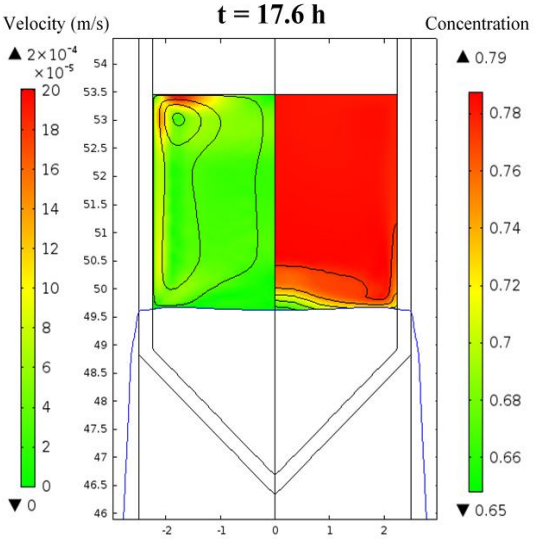
t = 17.6 h
Velocity (m/s)
Concentration

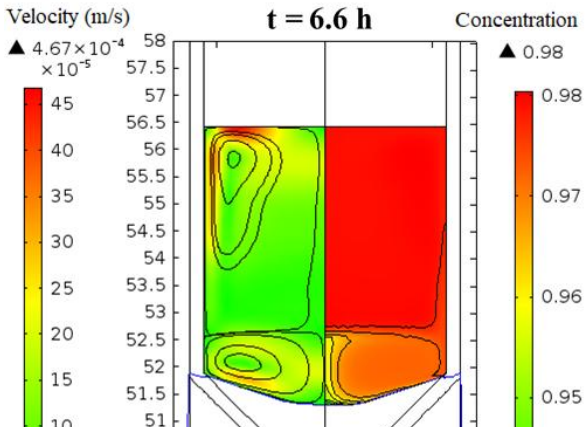
t = 6.6 h
Velocity (m/s)
Concentration

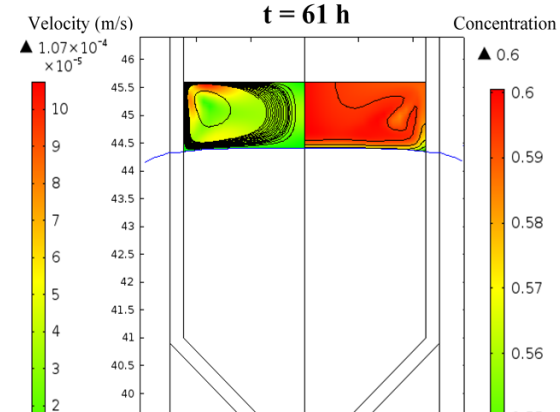
t = 61 h
Velocity (m/s)
Concentration

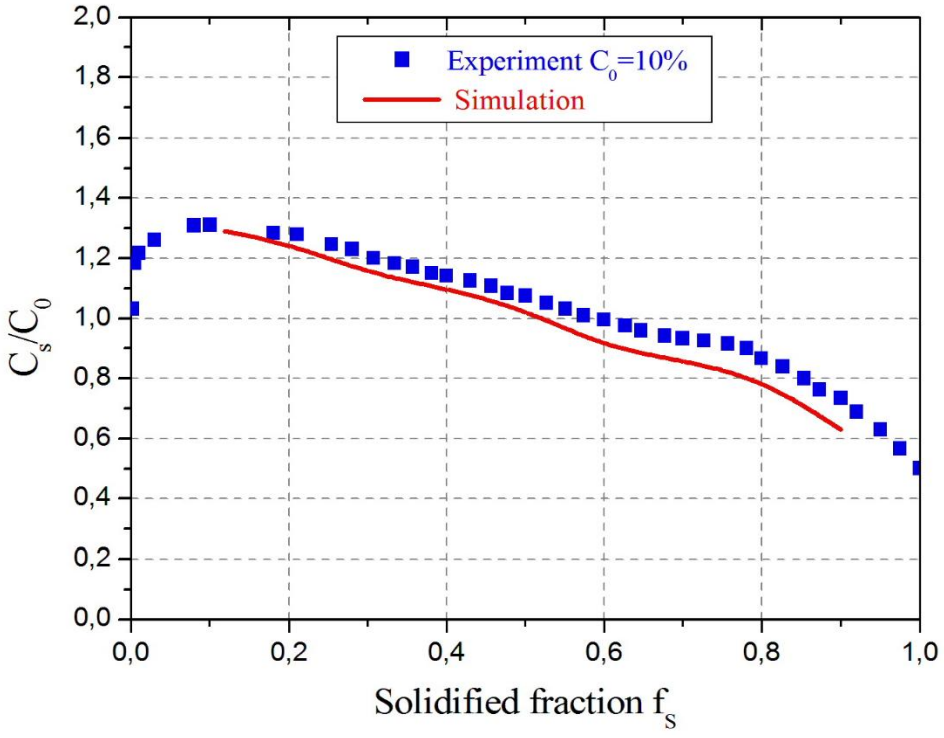

Fig. 3 Comparison between numerical computed Zn distribution (dimensionless concentration C_S/C_0) along the crystal axis and the measured profile. The dimensionless concentration C_S/C_0 is plotted versus the solidified fraction f_S.

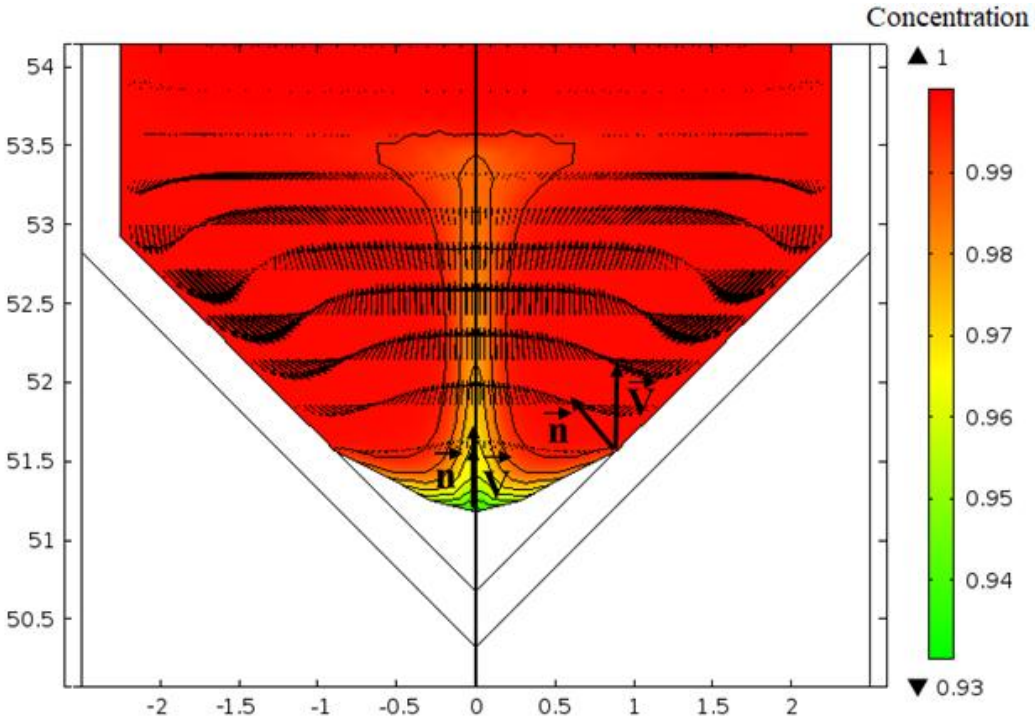

Fig. 4 Dimensionless concentration field (C/C_0), Zn isoconcentrations and the velocity field at the beginning of the solidification process

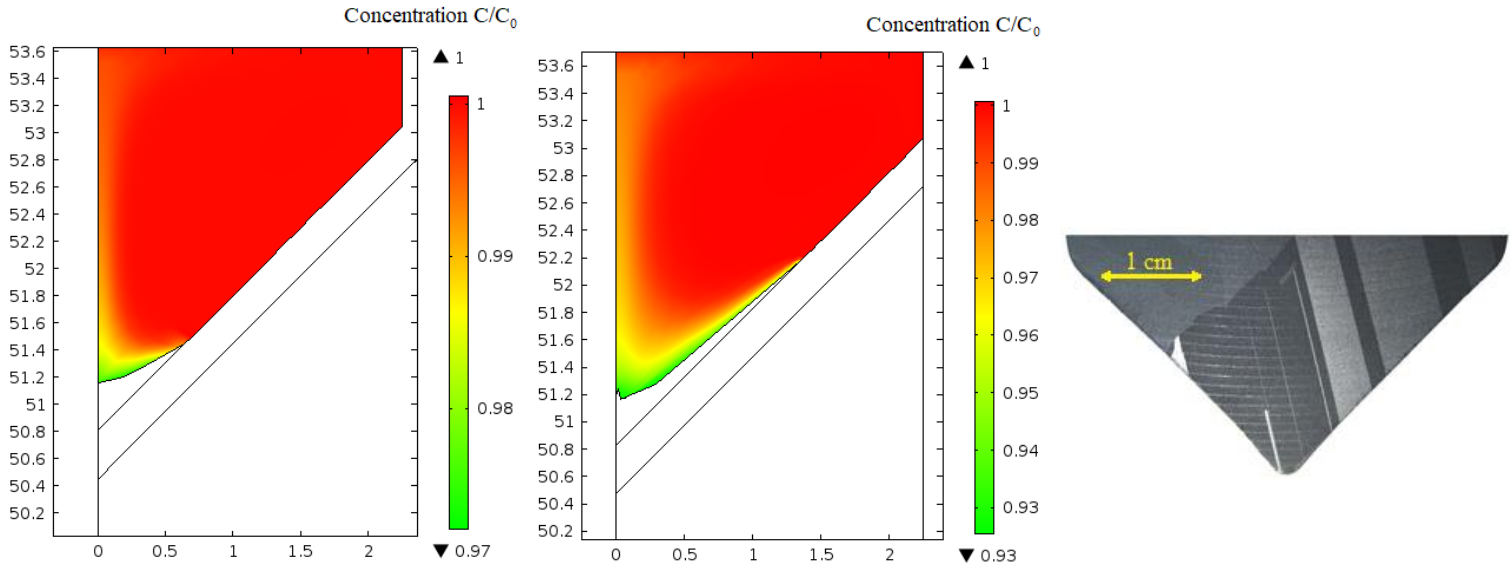

(a) (b) (c)

Fig. 5 (a) Dimensionless concentration field and the growth interface shape computed by neglecting the liquidus effect; (b) Dimensionless concentration field and the growth interface shape computed by accounting the liquidus effect; (c) Photograph showing large grains developing at the ampoule tip.

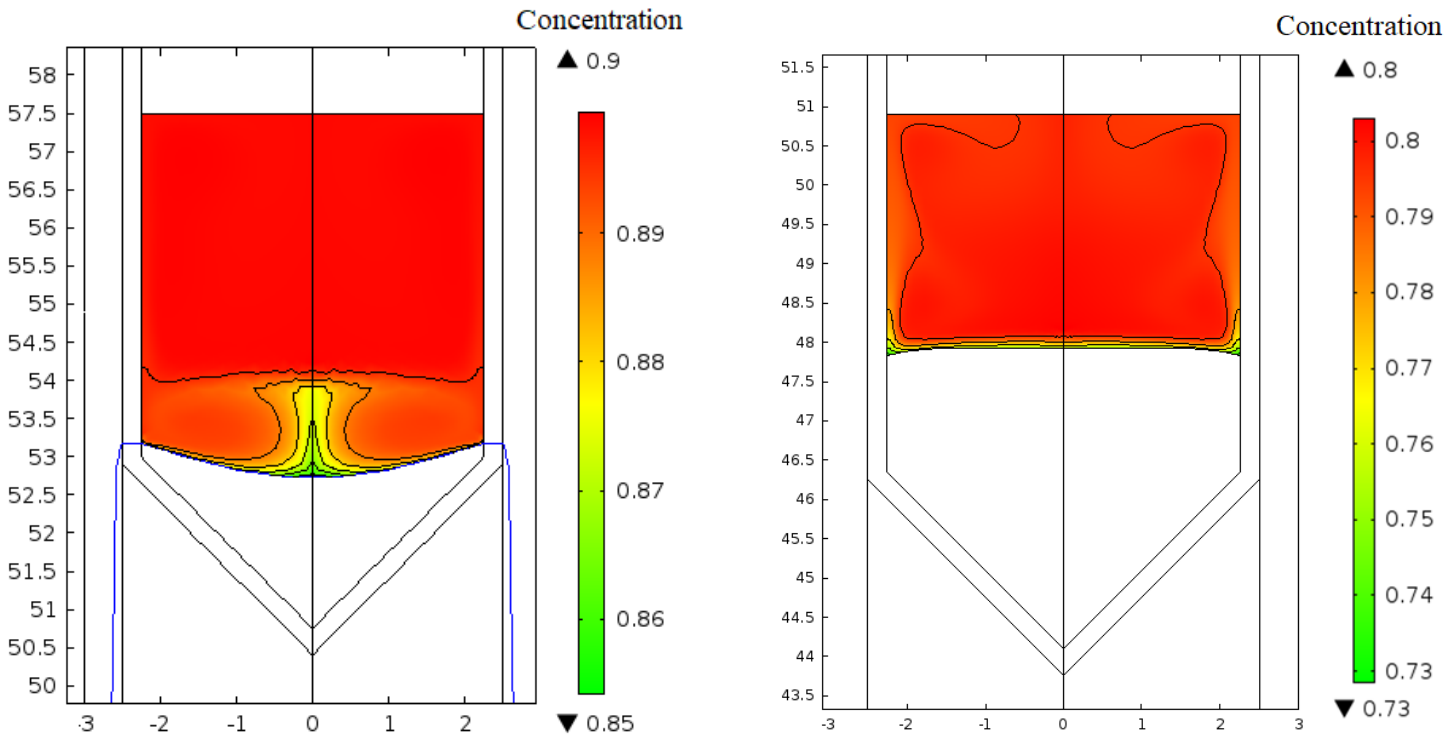

Fig. 6 Distribution of Zn (dimensionless concentration C/C_0) and isoconcentration contours in the liquid sample computed at two solidified fractions: $f_S = 0.29$ (a) and $f_S = 0.55$ (b).

(a)

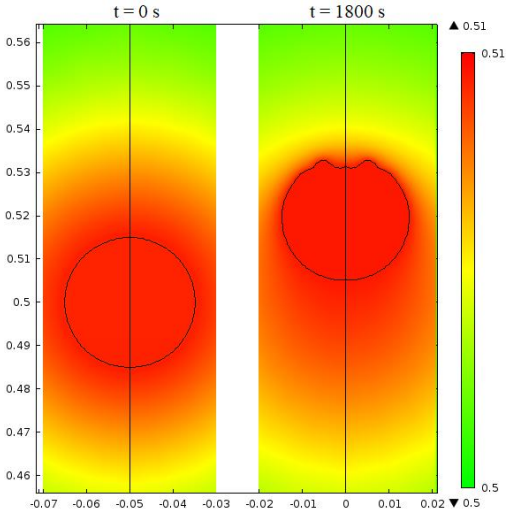
t = 0 s
t = 1800 s
▲ 0.51
0.51
0.5
▼ 0.5

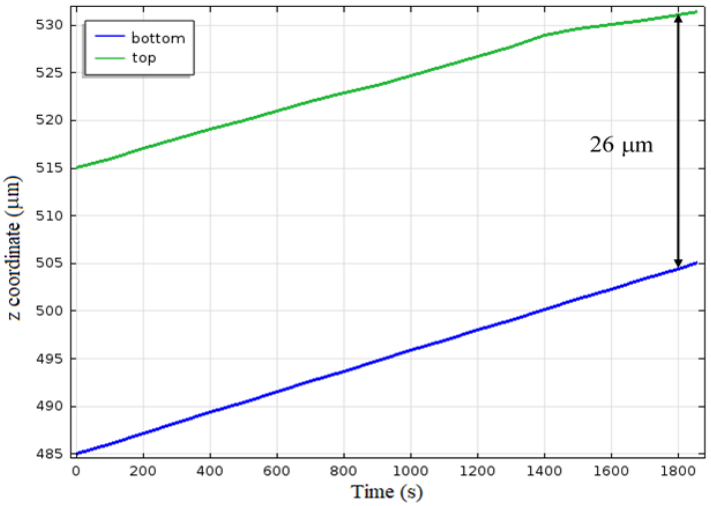
bottom
top
26 µm
z coordinate (µm)
Time (s)

(b)

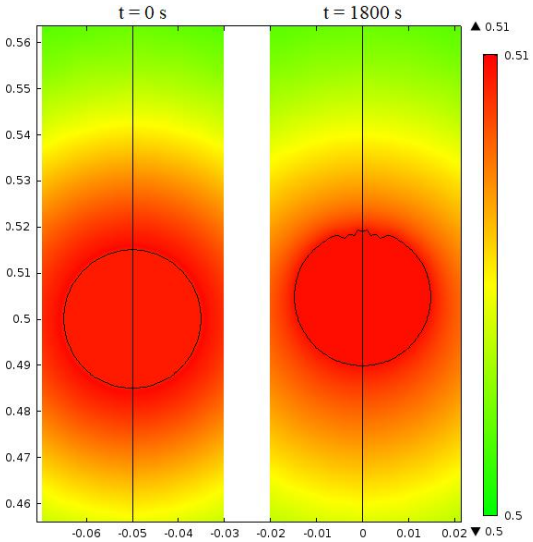
t = 0 s
t = 1800 s
▲ 0.51
0.51
0.5
▼ 0.5

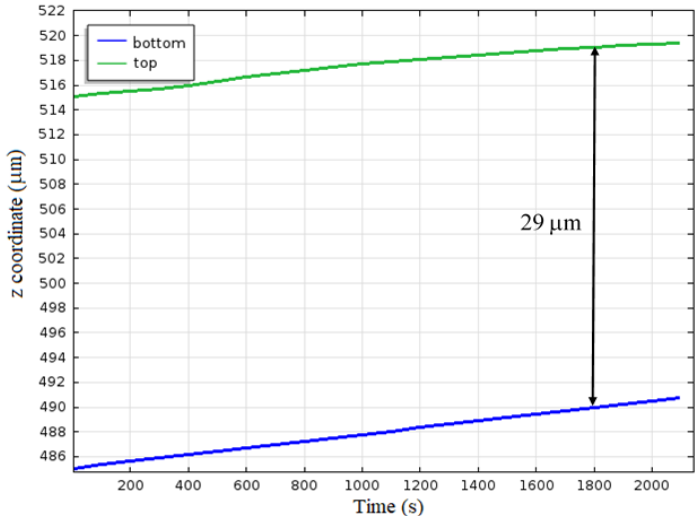
bottom
top
29 µm
z coordinate (µm)
Time (s)

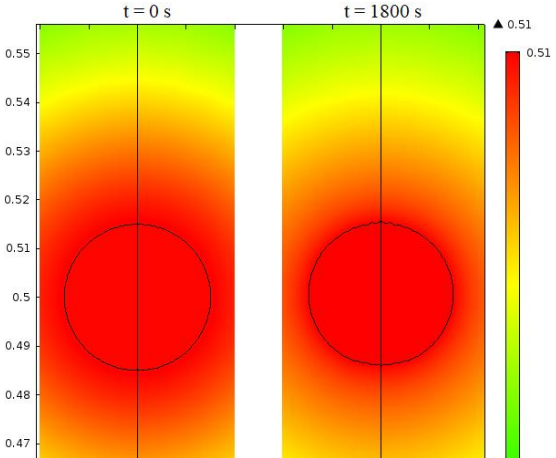
t = 0 s
t = 1800 s
▲ 0.51
0.51

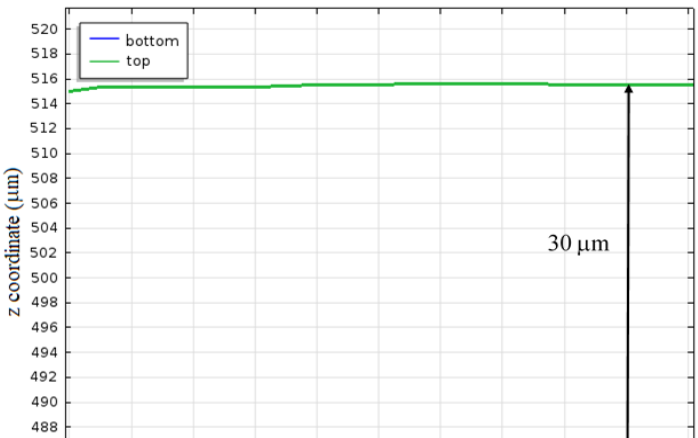
bottom
top
30 µm
z coordinate (µm)

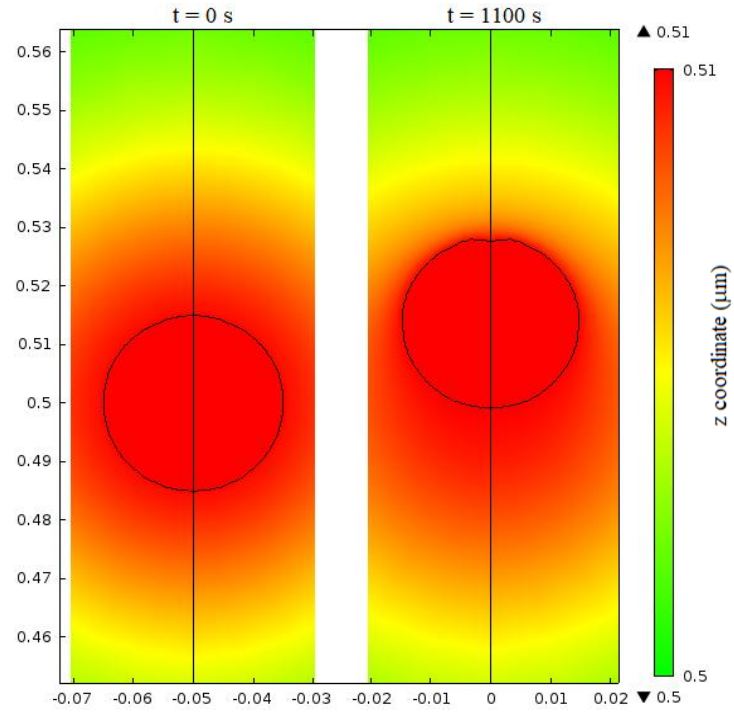
t = 0 s
t = 1100 s
▲ 0.51
0.51
0.5
▼ 0.5
0.56
0.55
0.54
0.53
0.52
0.51
0.5
0.49
0.48
0.47
0.46
-0.07
-0.06
-0.05
-0.04
-0.03
-0.02
-0.01
0
0.01
0.02

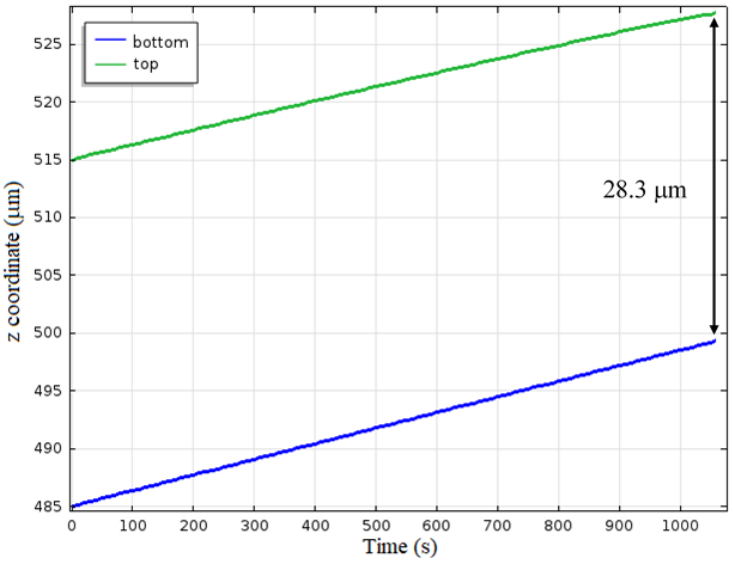
bottom
top
28.3 µm
z coordinate (µm)
Time (s)
525
520
515
510
505
500
495
490
485
0
100
200
300
400
500
600
700
800
900
1000

(a)

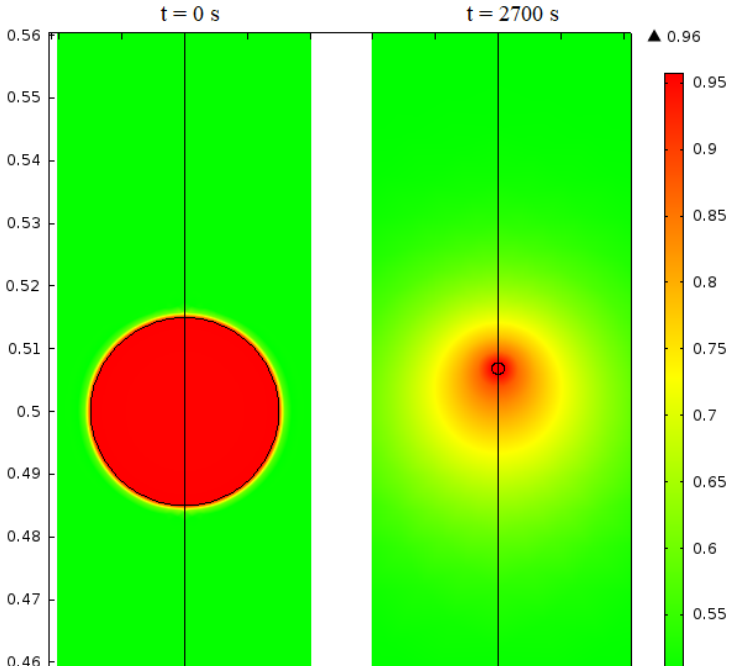
t = 0 s
t = 2700 s
▲ 0.96
0.95
0.9
0.85
0.8
0.75
0.7
0.65
0.6
0.55
0.56
0.55
0.54
0.53
0.52
0.51
0.5
0.49
0.48
0.47
0.46

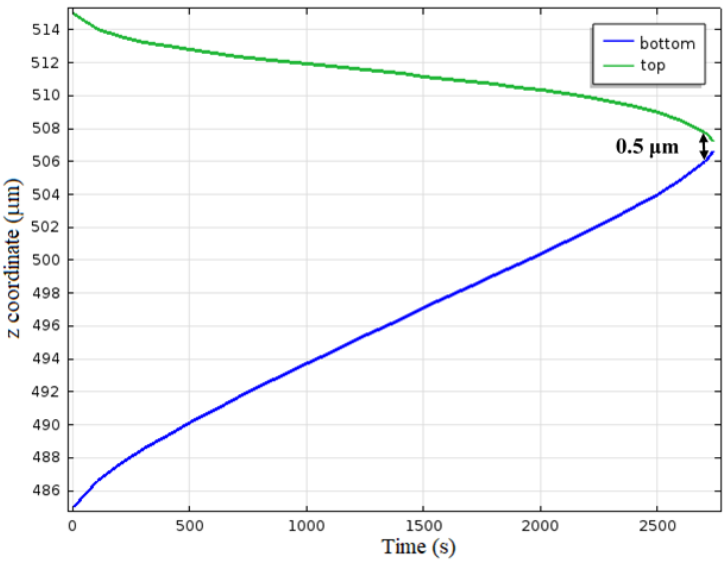
bottom
top
0.5 µm
z coordinate (µm)
Time (s)
514
512
510
508
506
504
502
500
498
496
494
492
490
488
486
0
500
1000
1500
2000
2500

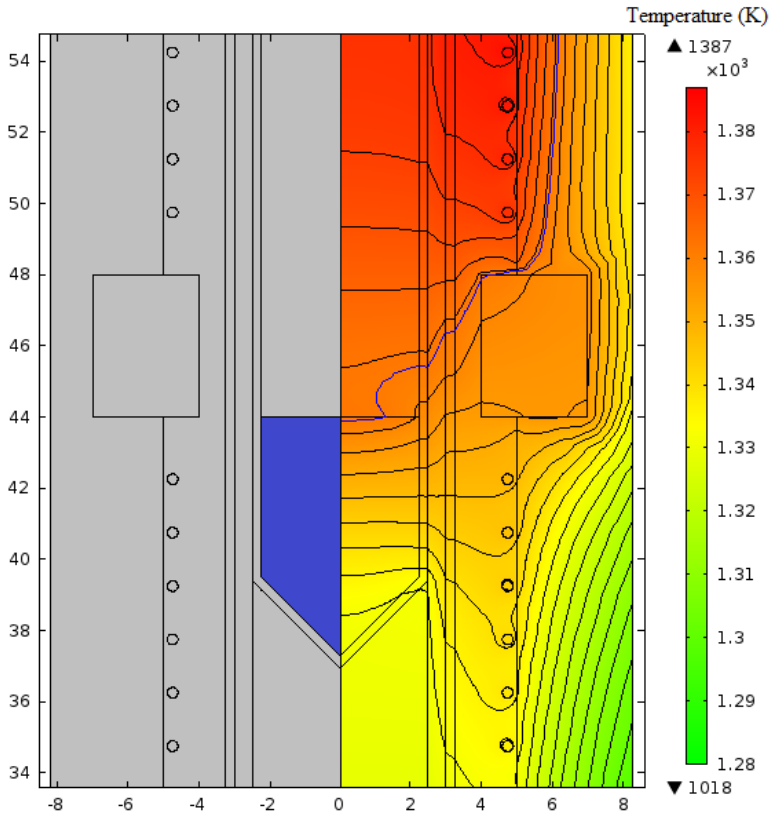
Temperature (K)
▲ 1387
×10³
1.38
1.37
1.36
1.35
1.34
1.33
1.32
1.31
1.3
1.29
1.28
▼ 1018

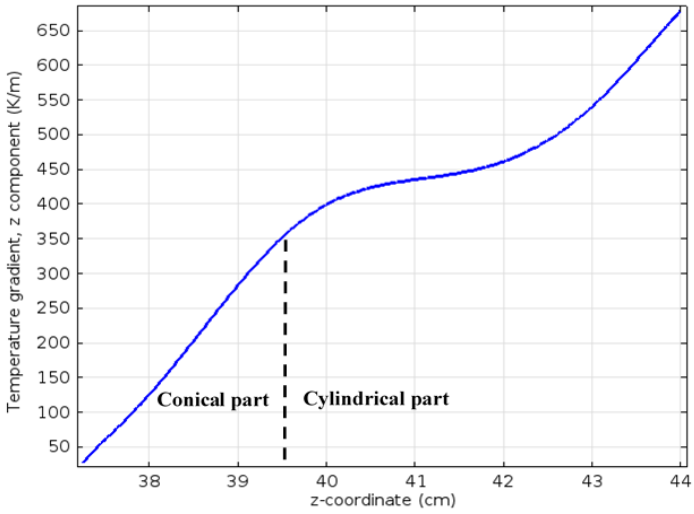
Temperature gradient, z component (K/m)
z-coordinate (cm)
Conical part
Cylindrical part

(a)

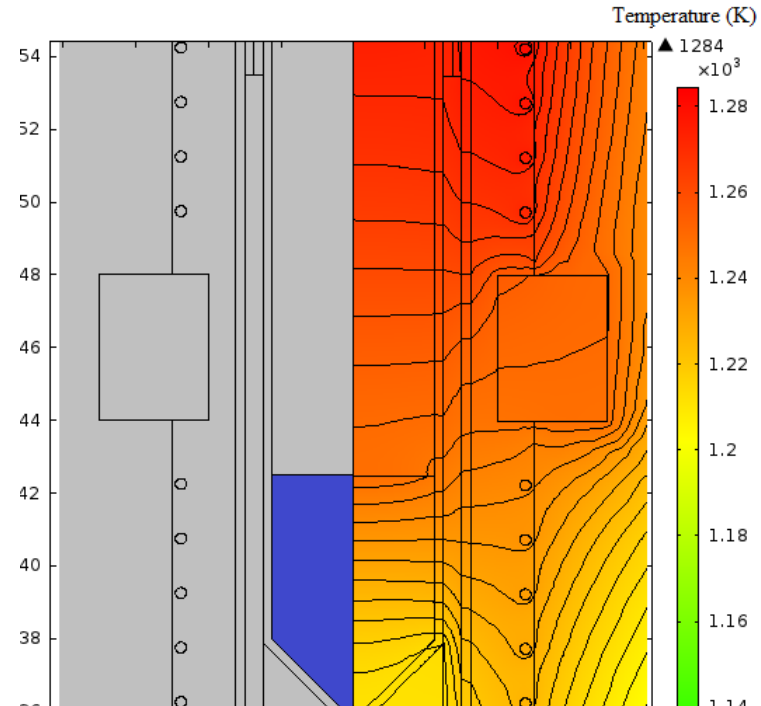
Temperature (K)
▲ 1284
×10³
1.28
1.26
1.24
1.22
1.2
1.18
1.16

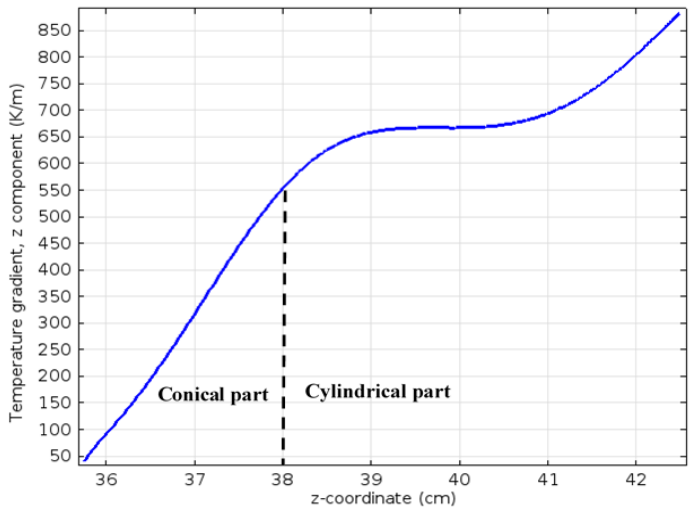
Temperature gradient, z component (K/m)
z-coordinate (cm)
Conical part
Cylindrical part